Journal of Magnetic Resonance 348 (2023) 107374

Contents lists available at ScienceDirect

Journal of Magnetic Resonance

journal homepage: www.elsevier.com/locate/jmr

Revealing impacts of electrolyte speciation on ionic charge storage in aluminum-quinone batteries by NMR spectroscopy

Leo W. Gordon, Jonah Wang, Robert J. Messinger *

Department of Chemical Engineering, The City College of New York, CUNY, 160 Convent Ave., New York, NY 10031, USA

ARTICLE INFO

Article history:
Received 6 December 2022
Revised 2 January 2023
Accepted 6 January 2023
Available online 9 January 2023

Keywords:
Aluminum-organic batteries
solid-state NMR
Dipolar-mediated NMR
Multiple-quantum NMR
Ionic liquids
Ionic liquid analogues
DFT calculations

ABSTRACT

Rechargeable aluminum-organic batteries are composed of earth-abundant, sustainable electrode materials while the molecular structures of the organic molecules can be controlled to tune their electrochemical properties. Aluminum metal batteries typically use electrolytes based on chloroaluminate ionic liquids or deep eutectic solvents that are comprised of polyatomic aluminum-containing species. Quinone-based organic electrodes store charge when chloroaluminous cations ($AlCl_2^+$) charge compensate their electrochemically reduced carbonyl groups, even when such cations are not natively present in the electrolyte. However, how ion speciation in the electrolyte affects the ion charge storage mechanism, and resultant battery performance, is not well understood. Here, we couple solid-state NMR spectroscopy with electrochemical and computational methods to show for the first time that electrolyte-dependent ion speciation significantly alters the molecular-level environments of the charge-compensating cations, which in turn influences battery properties. Using 1,5-dichloroanthraquinone (DCQ) for the first time as an organic electrode material, we utilize solid-state dipolar-mediated and multiple-quantum NMR experiments to elucidate distinct aluminum coordination environments upon discharge that depend significantly on electrolyte speciation. We relate DFT-calculated NMR parameters to experimentally determined quantities, revealing insights into their origins. The results establish that electrolyte ion speciation impacts the local environments of charge-compensating chloroaluminous cations and is a crucial design parameter for rechargeable aluminum-quinone batteries.

1. Introduction

Batteries composed of low-cost, safe, earth abundant, and highly recyclable materials are needed to secure the planet's future energy needs. Much of this requirement will be large-scale grid storage necessitated by intermittent renewable energy sources, such as wind and solar. Aluminum (Al) metal has many benefits as a battery electrode, including high earth crust abundance (8.23 wt%), large theoretical volumetric capacity (8046 mA h mL^{-1}), low cost, and inherent safety. Despite these advantages, aluminum batteries are still in their infancy, primarily because few electrolytes enable electroplating and stripping Al metal at room temperature. Rechargeable aluminum batteries currently use chloroaluminate ionic liquid (IL) and IL analogue (ILA) electrolytes, whose Lewis acidic mixtures remove the native oxide layer and enable reversible electroplating of Al metal.[1–6] However, chloroaluminate species are corrosive and reactive, while many positive electrode materials are not (electro)chemically stable with used with them.[7].

Organic battery electrode materials can be designed at a molecular level to tailor properties ranging from cell voltage to electrolyte compatibility. Aluminum-organic batteries are of particular interest due to the mutual benefits of abundance, safety, and low cost of the electrodes.[8–19] Aromatic quinones are attractive as battery electrodes due to their inherent electrochemical redox activity and weak intermolecular bonds that allow ion transport with low energetic barriers. Aluminum-quinone batteries have primarily been studied using Lewis acidic $AlCl_3$:[EMIm]Cl IL electrolytes, where aluminum is found as chloroaluminate $AlCl_4^-$ and $Al_2Cl_7^-$ anions. However, quinone-based cathodes in these electrolytes have been reported to store charge via the complexation of polyatomic chloroaluminous $AlCl_2^+$ cations,[8–11,15–17] as well as divalent $AlCl^{2+}$ [12,13] or even trivalent Al^{3+} [14]. The complexation of aluminum-containing cations to the organic quinone electrodes poses a key question: how do these electroactive cationic species form in an electrolyte natively containing only chloroaluminate anions? To date, just one study by Kao et al. [17] has been conducted on aluminum-quinone batteries using an alternative

* Corresponding author.
E-mail address: rmessinger@ccny.cuny.edu (R.J. Messinger).

https://doi.org/10.1016/j.jmr.2023.107374
1090-7807/

electrolyte, specifically the $AlCl_3$:urea ILA, where in addition to the chloroaluminate anions, neutral and cationic aluminum-containing species also exist: $AlCl_2[urea]_2^+$, $AlCl_3[urea]$, and $AlCl_3[urea]_2$.[3,20] The charge-compensating cation in this system was proposed to be $AlCl_2[urea]_2^+$, yet much remains to be understood about the ionic charge storage mechanisms when using these electrolyte systems. Understanding the fundamental mechanistic processes underpinning these emerging battery chemistries is crucial for their scientific and technological development.

Solid-state nuclear magnetic resonance (NMR) spectroscopy is uniquely suited for studying charge storage mechanisms in aluminum-organic batteries. Protons are abundant in the electroactive organic molecules, which can be characterized directly or used in heteronuclear dipolar-mediated NMR experiments to probe other nuclei.[21] The ^{27}Al nuclide is also highly sensitive as it is 100 % naturally abundant and has a high gyromagnetic ratio ($\gamma = 6.976 \times 10^7$ rad s^{-1} T^{-1}, receptivity of 1.22×10^3 relative to ^{13}C). Due to their quadrupolar nature (spin 5/2), ^{27}Al nuclei interact with local electric field gradients (EFGs), yielding complex quadrupolar lineshapes resulting from the second-order quadrupolar interactions that are not averaged out by MAS.[22–24] Information on aluminum symmetry and ligation is encoded within these quadrupolar lineshapes; therefore, measuring and understanding quadrupolar parameters can yield critical insights into local aluminum binding environments, such as those of charge-compensating polyatomic aluminum cations. Lastly, solid-state NMR enables analysis of heterogeneous battery electrodes containing both solid and residual liquid electrolyte, e.g., as recently demonstrated in Al-sulfur batteries.[25] The advantage is twofold: (i) solvent washing is mitigated which can otherwise alter the sample, while (ii) the mobile (liquid) species can be selectively filtered using dipolar-mediated experiments and/or by leveraging differences in nutation of the liquid and solid quadrupolar nuclei, revealing only the solid.[9,25] Recently, Gordon et al. [9] used multi-dimensional solid-state NMR spectroscopy, including dipolar filters, to measure experimentally the ionic and electronic charge storage mechanisms in an Al-quinone battery electrode (indanthrone quinone, INDQ), revealing electrochemical enolization and the tetrahedral nature of the charge-compensating chloroaluminous $AlCl_2^+$ cation upon complexation. To date, this remains the only solid-state NMR study of rechargeable Al-quinone battery systems.

Here, we perform multi-dimensional solid-state NMR measurements, in concert with electrochemical techniques and DFT calculations, on aluminum metal batteries using 1,5-dichloroanthraquinone (DCQ) as an organic cathode material to understand how electrolyte speciation affects the ionic charge storage mechanism up from the molecular level. DCQ was chosen as a small anthraquinone-based molecule as its behavior is expected to be generalizable to existing Al-organic battery literature using quinone-based electrodes, while its chlorine substituents result in modestly improved cell voltages compared to anthraquinone.[26] Three IL and ILA electrolytes were tested, which each contain unique ion speciations that are shown to result in different local environments and distributions of the polyatomic aluminum cations complexing to DCQ. We couple solid-state NMR measurements with DFT calculations to identify probable binding configurations of the charge-compensating ions and to understand the thermodynamics of competitive reaction mechanisms originating from different electrolyte species.

2. Results and Discussion

Three different electrolytes with unique ion speciations were compared to systematically test existing hypotheses of the Al-quinone charge storage mechanism: (i) $AlCl_3$:[EMIm]Cl (1.5:1 molar ratio), (ii) $AlCl_3$:urea (1.3:1 molar ratio), and (iii) $AlCl_3$:propionamide (1.3:1 molar ratio). The $AlCl_3$:[EMIm]Cl IL contains $Al_2Cl_7^-$ and $AlCl_4^-$, whereas the urea and propionamide (PA) ILAs contain $Al_2Cl_7^-$, $AlCl_4^-$, $AlCl_2L_2^+$, $AlCl_3L$ and $AlCl_3L_2$, where L = urea or propionamide, respectively.[3,27] It was previously proposed that electroactive chloroaluminous $AlCl_2^+$ cations are produced from $Al_2Cl_7^-$ in aluminum-quinone batteries using $AlCl_3$:[EMIm]Cl

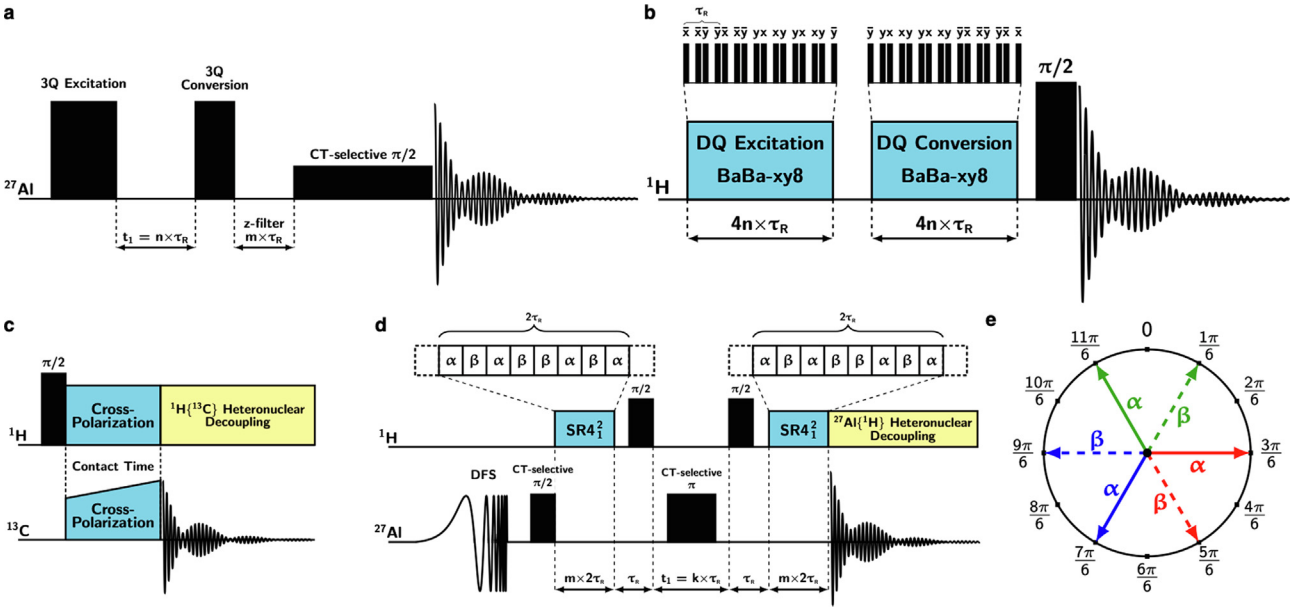

Fig. 1. Solid-state NMR experiments used in this work. (a) Three-pulse $^{27}Al\{^{27}Al\}$ multiple-quantum MAS (MQ-MAS) pulse sequence. (b) $^1H\{^1H\}$ dipolar-mediated double-quantum filter (D-DQF) pulse sequence using BaBa-xy8 blocks [28] for double-quantum (DQ) excitation and conversion. (c) $^{13}C\{^1H\}$ cross-polarization-MAS (CP-MAS) pulse sequence with ramped X-channel power. (d) $^{27}Al\{^1H\}$ dipolar-mediated heteronuclear multiple-quantum correlation (D-HMQC) pulse sequence with $SR4_1^2$ recoupling blocks [29,30] and a double-frequency sweep (DFS) preparatory pulse. (e) α and β pulse phases in the $SR4_1^2$ scheme. The sequence increments every-two rotor periods from red-blue-green for a six-rotor-period supercycle. A minimum of two rotor periods are required for recoupling, and optimally multiples of six rotor periods should be used to complete the full supercycle. (For interpretation of the references to colour in this figure legend, the reader is referred to the web version of this article.)

electrolytes.[9,15] However, in electrolytes that contain polyatomic $AlCl_2L_2^+$ cations alongside $Al_2Cl_7^-$ anions, such as the ILAs, it is unclear how the ion charge storage reaction would proceed and what competition would exist in generating ions from the native electrolyte species. To study these effects up from the molecular level, solid-state NMR experiments were performed on DCQ electrodes electrochemically cycled in the different electrolytes, including dipolar-mediated and multiple-quantum NMR measurements (Fig. 1), the results of which are discussed below.

Electrochemical Cycling of Al-DCQ Cells. Galvanostatic cycling was first performed on Al-DCQ cells with each of the three electrolytes to characterize their electrochemical properties (Fig. 2). The theoretical capacity of a DCQ electrode is expected to be 193.4 mA h g^{-1}, assuming a two-electron reaction per molecule of DCQ. These cells were fabricated without performance optimization measures such as melt-infused carbons[13] or functionalized separators [31] as our intention was to study how electrolyte speciation affects the ion charge storage mechanism. Based on results from similar anthraquinone-based electrode materials, the carbonyl groups of DCQ are electrochemically reduced upon discharge in an enolization reaction and are subsequently charge-compensated by $AlCl_2^+$ ions.[9,11,15,16].

DCQ discharged in the $AlCl_3$:[EMIm]Cl electrolyte yielded an initial specific discharge capacity of 200 mA h g^{-1}, close to the theoretical capacity, with a single, flat plateau at a potential of 1.0 V (Fig. 2a). The discharge capacities reduced upon further cycling, possibly a result of dissolution of partially charged DCQ molecules in the electrolyte,[31] which could be mitigated by oligomerizing or polymerizing DCQ. The first charge step had three distinct plateaus with an overall specific capacity more than double that of the discharge. The two higher potential plateaus are of unknown origin and are reduced in subsequent charges, while the overall charge capacity becomes commensurate with the reduced discharge capacities. For DCQ discharged in the ILAs, the initial discharge specific capacities are lower compared to the IL: 68 mA h g^{-1} for $AlCl_3$:urea (Fig. 2b) and 120 mA h g^{-1} for $AlCl_3$:PA (Fig. 2c). In the $AlCl_3$:urea electrolyte, the flat discharge plateaus at 1.0 V are followed by a long sloping profile. The $AlCl_3$:PA electrolyte demonstrates a similar behavior after cycle 1, though the sloping part of the curve is more pronounced. The sloping discharge profiles may be a result of disorder imparted to the electrode following the initial discharge. Charge reactions for both ILAs also exhibit higher potential plateaus, similar to DCQ discharged in $AlCl_3$:[EMIm]Cl. For all electrolytes, the overpotential for ion removal upon charge may be associated with ion-assisted solvation of complexed $AlCl_2^+$ ions and mass-transport limitations.[32] The galvanostatic cycling tests were performed at 60 ℃ to mitigate impacts from differences in electrolyte conductivity and enhance electrochemical kinetics, enabling better comparisons of the ion charge storage mechanisms.[20,33,34].

Cyclic voltammetry (CV) experiments followed similar trends to that of the galvanostatic cycling (Fig. S1). For example, the smallest currents were observed with the $AlCl_3$:urea electrolyte where as the $AlCl_3$:PA electrolyte yielded broad peaks commensurate with the sloping plateaus observed in its galvanostatic cycling. Interestingly, two sets of redox peaks are observed in the CV curves for the $AlCl_3$:[EMIm]Cl electrolyte, a result also observed for indanthrone quinone in the same electrolyte.[9] The reduction peak at ca. 0.3 V may be associated with $EMIm^+$ cation decomposition and is discussed further below.

Characterization of Pristine DCQ. Solid-state ^1H and ^{13}C NMR spectra of pristine DCQ powder were acquired, alongside powder X-ray diffraction (XRD) measurements, to characterize the material as a baseline (Fig. 3).

The ^1H spin-echo NMR spectrum (Fig. 3a) yields one broad signal in the aromatic region. Interestingly, the ^1H T_1 relaxation time

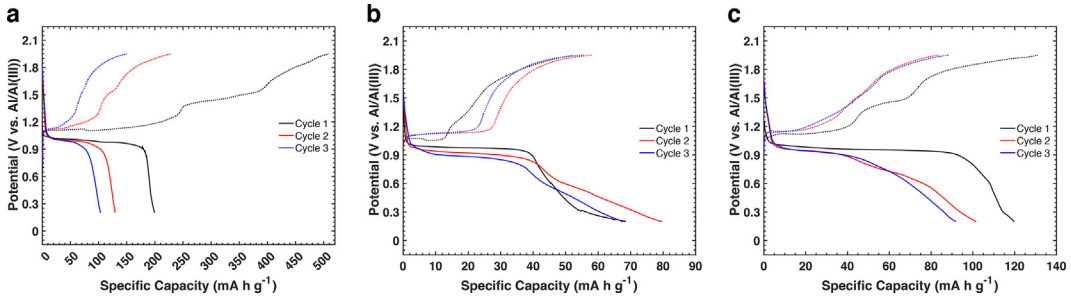

Fig. 2. Galvanostatic cycling curves of Al-DCQ cells using (a) $AlCl_3$:[EMIm]Cl (1.5:1), (b) $AlCl_3$:urea (1.3:1), and (c) $AlCl_3$:PA (1.3:1) electrolytes performed at 10 mA g^{-1} and 60 ℃. Note the differences in the scale of the *x*-axes.

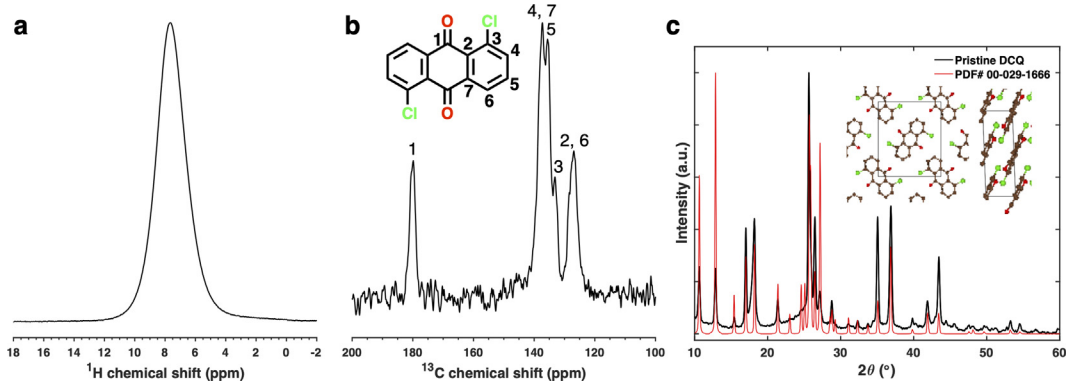

Fig. 3. Solid-state (a) ^1H spin-echo and (b) $^{13}C\{^1H\}$ CP-MAS NMR spectra of pristine DCQ powder acquired at 35 kHz MAS and 14.1 T. Inset in (b): molecular structure of DCQ with ^{13}C signal assignments.[36] (c) Powder XRD pattern of a pristine DCQ electrode (black) shown with the simulated pattern (red, PDF# 00–029-1666). Inset: crystal structure of DCQ. (For interpretation of the references to colour in this figure legend, the reader is referred to the web version of this article.)

is 655 s. This long longitudinal relaxation is typical for a rigid, crystalline material, as the DCQ molecules are highly ordered with strong intermolecular interactions due to both π-π stacking and halogen bonding.[35] The $^{13}C\{^1H\}$ cross-polarization MAS (CP-MAS) NMR spectrum (Fig. 3b; pulse sequence in Fig. 1c) shows ^{13}C signals in three groups: carbonyl (carbon '1′), aromatic ('3′-'6′), and quaternary ('2′, '7′).[36] The powder XRD pattern (Fig. 3c) shows the crystallinity of DCQ, consistent with its long ^1H T_1 relaxation time. The intense reflection at a 2θ angle of 25.65°, corresponding to a *d*-spacing of 3.56 Å, represents the interlayer spacing.

Understanding Electrolyte Species by NMR. Liquid-state ^{27}Al single-pulse experiments were acquired under quantitative conditions to determine the aluminum species in the pristine electrolytes for both the Lewis acidic ratios (Fig. 4a,d,g) used in electrochemical cells as well as their Lewis neutral equivalents (Fig. 4b,e,h). The aluminum species expected for all three electrolytes were observed: $AlCl_3$:[EMIm] contains $AlCl_4^-$ and $Al_2Cl_7^-$,[33,37] whereas $AlCl_3$:urea[3,38] and $AlCl_3$:PA[27,34,39,40] contain $AlCl_4^-$, $AlCl_2L_2^+$, $AlCl_3L$, and $AlCl_3L_2$ (where L is the ligand, either urea or propionamide), as well as $Al_2Cl_7^-$. Significant line broadening is observed in the ^{27}Al NMR spectra for the Lewis acidic mixtures (Fig. 4a,d,g), a result of rapid chemical exchange on the NMR timescale facilitated by the presence of $Al_2Cl_7^-$. This effect is particularly pronounced for the $AlCl_3$:urea electrolyte, where all ^{27}Al signals merge into one broad signal.[27,33].

DCQ electrodes were discharged in Al-DCQ cells (10 mA g^{-1}, cycle 3), harvested, and packed into NMR rotors along with residual liquid electrolyte trapped within the electrode pores, uniquely enabling simultaneous, nuclide-specific characterization of both the solid discharged electrode and liquid electrolyte remnants. The solid-state ^{27}Al spin-echo NMR experiments (Fig. 4c,f,i) were acquired with rf pulse lengths of π/2 (with respect to 1 M aqueous $Al(NO_3)_3$), exciting predominantly the liquid electrolyte signals because (i) the solid ^{27}Al signals are quadrupolar (see below) and nutate at a faster rate [41,42], resulting in poor excitation over the two-pulse sequence, coupled with (ii) the faster transverse T_2 relaxation times of the solid ^{27}Al environments, enabling the experiment to work as a transverse relaxation filter. Thus, to a first approximation, the ^{27}Al spin-echo NMR measurements selectively analyzes the residual liquid electrolyte in the pores of the solid discharged electrodes, which can be compared to the neat Lewis acidic electrolytes and their Lewis neutral equivalents. Liquid-state ^1H single-pulse NMR spectra of the pristine electrolytes yielded ^1H signals associated with $EMIm^+$ cations, urea, or propionamide, as expected (Fig. S2).

Analyzing the ^{27}Al NMR spectra reveals insights into aluminum ion speciation in the residual electrolytes after discharge. The liquid-state ^{27}Al spin-echo NMR spectrum of the Lewis acidic $AlCl_3$:[EMIm]Cl electrolyte (Fig. 4a) exhibits ^{27}Al signals corresponding to $AlCl_4^-$ (103 ppm) and $Al_2Cl_7^-$ (98 ppm), whereas the Lewis neutral electrolyte (Fig. 4b) contains only $AlCl_4^-$. The solid-state ^{27}Al spin-echo NMR spectrum of the discharged DCQ electrode reveals that the residual electrolyte contained both $Al_2Cl_7^-$, and $AlCl_4^-$ (Fig. 4c), indicating that it retains Lewis acidity upon discharge. The liquid-state ^{27}Al single-pulse NMR spectra of the Lewis acidic $AlCl_3$:urea and $AlCl_3$:PA ILAs (Fig. 4d,g) exhibit broad lineshapes due to rapid chemical exchange facilitated by $Al_2Cl_7^-$ in the electrolytes, as noted above. The liquid-state ^{27}Al NMR spectra of the Lewis neutral ILAs (Fig. 4e,h) contain much sharper signals and bear striking resemblances to the solid-state ^{27}Al spin-echo NMR spectra of the residual liquid from DCQ electrodes discharged in the respective electrolytes (Fig. 4f,i), establishing that the electrochemical discharge process consumes $Al_2Cl_7^-$. This important result reveals that the Lewis acidic chloroaluminate electrolytes lose Lewis acidity during cycling, becoming more Lewis neutral upon

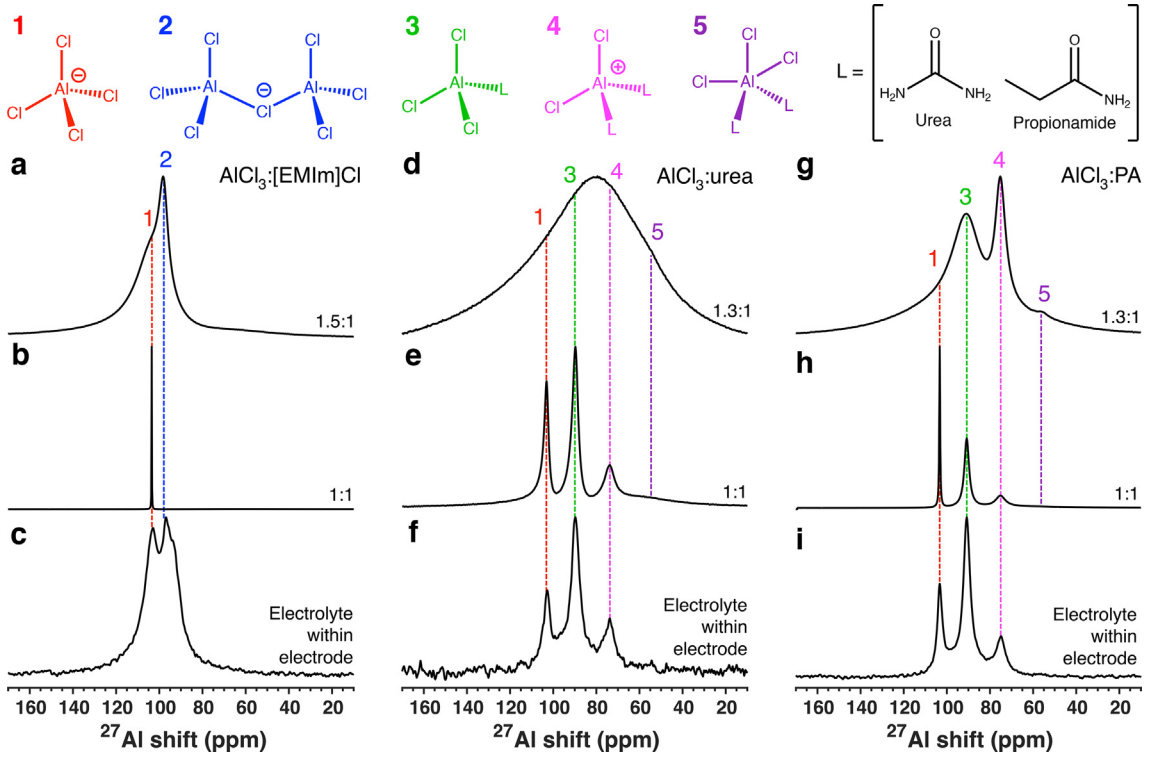

Fig. 4. Liquid-state ^{27}Al NMR spectra of Lewis acidic (a) $AlCl_3$:[EMIm]Cl (1.5:1), (d) $AlCl_3$:urea (1.3:1), and (g) $AlCl_3$:PA (1.3:1) electrolytes, and (b, e, h) their Lewis neutral equivalents (1:1), acquired at 7.05 T. (c, f, i) Solid-state ^{27}Al spin-echo NMR spectra of DCQ electrodes after galvanostatic discharge (10 mA g^{-1}, cycle 3), revealing predominantly residual liquid electrolyte within the pores, acquired at 40 kHz MAS and 14.1 T. Molecular structures of electrolyte species are shown and their corresponding ^{27}Al signal assignments are indicated on the NMR spectra.

full discharge in DCQ cells, with greater consequence for the ILA electrolytes that have less $Al_2Cl_7^-$ overall. This finding may help to explain the lower specific capacities and worse electrochemical performance of the ILA electrolytes compared to the Lewis acidic $AlCl_3$:[EMIm]Cl IL electrolyte.

Molecular-Level Environments of Aluminum Discharge Products. Due to the overlap of ^{27}Al NMR signals from solid and liquid species in the solid-state NMR spectra of the discharged electrodes, solid-state ^{27}Al{^{1}H} and ^{1}H{^{1}H} dipolar-mediated NMR techniques were used to selectively probe the solid aluminum discharge products. These dipolar filters depend upon the through-space magnetic dipole–dipole interactions between nuclear spins, which in turn depend upon (i) through-space internuclear distances (probing sub-nanometer length scales) and (ii) relative molecular mobilities. Dipolar-mediated correlation or filtering experiments will not reveal nuclear spins that are far apart (>1 nm) or experience rapid isotropic mobilities that average away the dipolar interactions. Here, we use solid-state ^{27}Al{^{1}H} dipolar-mediated heteronuclear multiple-quantum correlation (D-HMQC) NMR experiments using the symmetry-based $SR4_1^2$ sequence (Fig. 1d,e), which reveal ^{27}Al signals that are dipole–dipole-coupled with, and hence in close molecular proximity to, the ^{1}H signals of the DCQ molecules. This experiment thus reveals specifically the ^{27}Al signals associated with the solid Al-DCQ discharge products. 2D ^{27}Al{^{1}H} D-HMQC NMR spectra (Fig. 5a,e,i) measure through-space interactions between ^{27}Al and ^{1}H nuclei in different molecular-level environments. Separately acquired 1D ^{27}Al{^{1}H} D-HQMC spectra (Fig. 5b,f,j) acquired with greater signal-to-noise than the 1D projections are plotted along the horizontal axis, along with solid-state ^{27}Al single-pulse spectra (Fig. 5c,g,k) acquired under quantitative conditions ($\pi/12$ pulse, fully relaxed between scans) that show both solid and liquid signals. In addition, 1D ^{1}H{^{1}H} dipolar-mediated double-quantum-filtered (D-DQF) experiments using the BaBa-xy8 sequence (Fig. 5d,h,l; pulse sequence in Fig. 1b) are plotted along the vertical axis, which were used to filter the proton signals of residual electrolyte and reveal only solid ^{1}H signals.

The solid-state 2D ^{27}Al{^{1}H} D-HMQC NMR spectrum of DCQ discharged in Lewis acidic $AlCl_3$:[EMIm]Cl electrolyte (Fig. 5a) yielded 2D correlated signal intensities between the ^{27}Al environments in the tetrahedral shift region at ca. 91 ppm (environment I) and 75 ppm (environment II) and the aromatic ^{1}H environments centered at 7.5 ppm associated with DCQ, establishing their subnanometer-scale proximities. The 1D ^{27}Al{^{1}H} D-HMQC spectrum (Fig. 5b) reveals that the two ^{27}Al environments, which correspond to distinct tetrahedrally-coordinated solid discharge products, exhibit complex lineshapes indicative of ordered quadrupolar environments (confirmed by 2D ^{27}Al{^{27}Al} MQ-MAS experiments below). These two ^{27}Al environments are also observable in the quantitative ^{27}Al single-pulse spectrum (Fig. 5c), along with signals corresponding to residual liquid electrolyte species that are not observable in the ^{27}Al{^{1}H} D-HMQC experiments due to rapid molecular mobilities. The aromatic ^{1}H signals centered at 7.5 ppm in the ^{1}H{^{1}H} D-DQF spectrum (Fig. 5d) correspond to the ^{1}H shift of DCQ protons (Fig. 3a). There are additional ^{1}H signals at 1.4, 1.6, 3.8, 4.0, 7.2, and 8.2 ppm that exhibit heteronuclear ^{1}H–^{27}Al dipole–dipole interactions with ^{27}Al environments I and II, which are associated with $EMIm^+$ cations and any of its electrochemical degradation products.[9,43] Thus, $EMIm^+$ cations are also immobilized and in close molecular proximity to coordinated aluminum species.

An identical suite of solid-state NMR experiments acquired on DCQ discharged in the Lewis acidic $AlCl_3$:urea (Fig. 5e-h) and $AlCl_3$:PA (Fig. 5i-l) ILAs reveal key differences that yield insights into the role of the organic electrolyte components (urea, PA) toward the resultant molecular environments of the charge-compensating chloroaluminous cations. For the $AlCl_3$:urea electrolyte, 2D ^{27}Al{^{1}H} D-HMQC spectrum (Fig. 5e) also exhibits 2D correlated signal intensity between ^{27}Al signals associated with environments I and II and the DCQ ^{1}H signals at 7.5 ppm, establishing their mutual interactions. The 1D ^{27}Al{^{1}H} D-HMQC spectrum (Fig. 5f) clearly shows both distinct ^{27}Al environments. Curiously, for DCQ discharged in the $AlCl_3$:PA electrolyte, the solid-state 1D ^{27}Al{^{1}H} D-HMQC spectrum (Fig. 5j) reveals only one ^{27}Al signal (environment II). While the origin of this difference is not unknown, it must be linked to the structure of PA, which is more sterically bulky and hydrophobic compared to urea. The quantitative ^{27}Al single-pulse spectra (Fig. 5g,k) indicate the Lewis neutral nature of the residual liquid electrolytes and highlight the effectiveness of the dipolar-mediated experiments in filtering out the mobile liquid signals. Lastly, both the ^{1}H{^{1}H} D-DQF spectra (Fig. 5h,l) and 2D ^{27}Al{^{1}H} D-HMQC spectra (Fig. 5e,i) do not reveal the presence of apprecia-

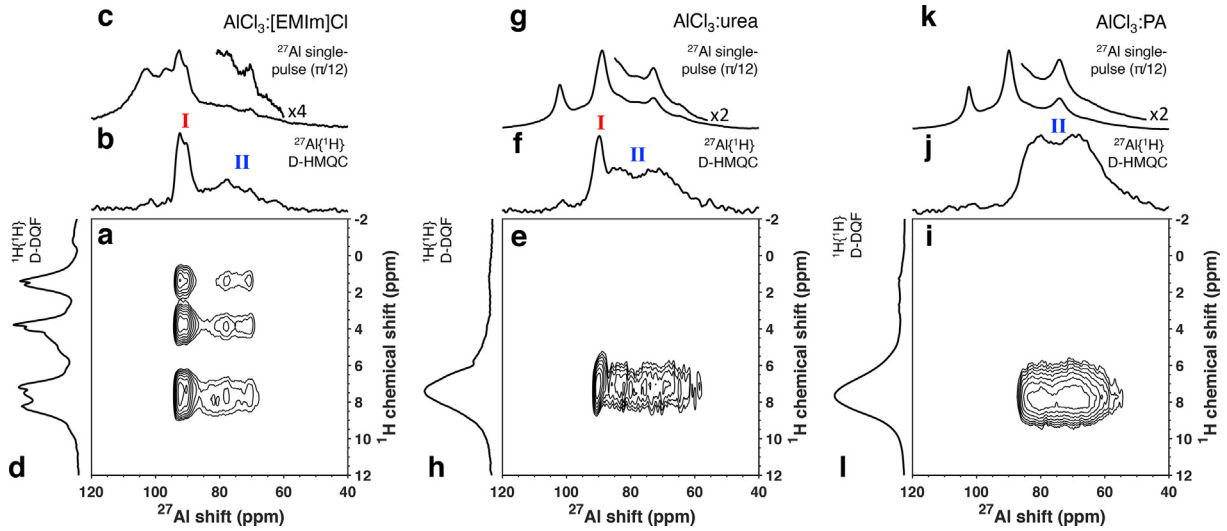

Fig. 5. Solid-state (a,e,i) 2D ^{27}Al{^{1}H} D-HMQC ($SR4_1^2$) NMR spectra, (b,f,j) 1D ^{27}Al{^{1}H} D-HMQC ($SR4_1^2$) NMR spectra, (c,g,k) 1D ^{27}Al single-pulse ($\pi/12$) NMR spectra, and (d,h,l) 1D ^{1}H{^{1}H} D-DQF (BaBa-xy8) NMR spectra of DCQ electrodes after galvanostatic discharge (10 mA g^{-1}, cycle 3) using (a-d) $AlCl_3$:[EMIm]Cl (1.5:1), (e-h) $AlCl_3$:urea (1.3:1), and (i-l) $AlCl_3$:PA (1.3:1) electrolytes, acquired at 40 kHz MAS and 14.1 T. The quadrupolar ^{27}Al environments I (red) and II (blue) are associated with $AlCl_2^+$ complexed to DCQ. (For interpretation of the references to colour in this figure legend, the reader is referred to the web version of this article.)

ble ^{1}H signals from $AlCl_3L$, $AlCl_3L_2$, or $AlCl_2L_2^+$ species in the solid phase, or their interactions with aluminum environments bound to DCQ, unlike the $EMIm^+$ cations.

To confirm the quadrupolar nature of the ^{27}Al environments and understand their lineshapes, a 2D ^{27}Al{^{27}Al} multiple-quantum MAS (MQ-MAS) NMR experiment (pulse sequence in Fig. 1a) was performed on the DCQ discharged in Lewis acidic $AlCl_3$:[EMIm]Cl electrolyte. The 2D ^{27}Al{^{27}Al} MQ-MAS spectrum (Fig. 6a) reveals two ^{27}Al signals with distinct quadrupolar lineshapes that are partially overlapping signals in the MAS dimension (Fig. 6b) but resolved in the isotropic dimension of the 2D spectrum. Slices were taken through the ^{27}Al signals in the isotropic dimension and the individual lineshapes were fitted using DMFit [44] to obtain their NMR parameters. The simulated quadrupolar lineshapes using these parameters are shown (Fig. 6c). Environment I (96.2 ppm, isotropic dimension) had a quadrupolar coupling constant C_Q of ca. 3.5 MHz and an asymmetry parameter η of 0.32, while environment II (98.8 ppm, isotropic dimension) had a C_Q of ca. 7.7 MHz and η of 0.59. Given the symmetrical structure of DCQ, it is interesting that two distinct ^{27}Al environments are observed. The complexing ion is expected to be $AlCl_2^+$, based on the tetrahedral coordination environment of Al; therefore, there must exist at least two locally stable configurations of $AlCl_2^+$ with distinct EFGs. Furthermore, these environments can be affected by electrolyte ion speciation, as DCQ discharged in Lewis acidic $AlCl_3$:PA electrolyte did not exhibit a ^{27}Al signal similar to environment I, as discussed above.

DFT Calculations Establish Links Between Physical Properties and NMR Parameters. To gain further insight into the origin of the different ^{27}Al environments and their quadrupolar lineshapes, DFT calculations were performed on systems of quinones with chloroaluminous $AlCl_2^+$ cations in different spatial positions and coordination environments.[45] DFT-calculated chemical shielding and EFG tensors were used to predict the ^{27}Al shifts and quadrupolar coupling constants, enabling comparisons to experimental data. For the calculations, *p*-benzoquinone (BQ) was used in lieu of DCQ as a general model for quinones and to reduce computational expense. $AlCl_2^+$ species were aligned with BQ oxygen atoms and placed between two BQ molecules, where the BQ molecules lied flat in the *x*-*y* plane. Interlayer spacing between the quinones (*z*-axis) and lateral spacing of the $AlCl_2^+$ ions (*y*-axis) were independently varied (Fig. 7a,b). The resultant total ^{27}Al isotropic shifts and quadrupolar coupling constants are plotted as mean values for each interlayer spacing, averaged over $AlCl_2^+$ lateral displacements of 1, 1.25, 1.5, 1.75, 2, and 2.25 Å with respect to the complexing quinone oxygen, with the range of values and standard deviations shown as lighter and darker shaded areas, respectively (Fig. 7c).

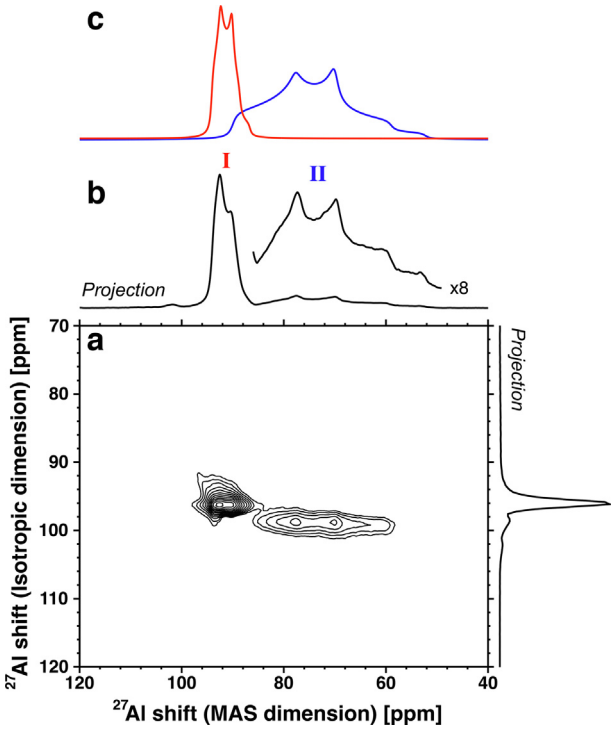

Fig. 6. (a) 2D solid-state ^{27}Al{^{27}Al} MQ-MAS NMR spectrum of a DCQ electrode after galvanostatic discharge (10 mA g^{-1}, cycle 3) in $AlCl_3$:[EMIm]Cl (1.5:1) electrolyte and (b) 1D ^{27}Al quadrupolar MQ-MAS skyline projection, acquired at 40 kHz MAS and 14.1 T, with ^{27}Al environments I (red) and II (blue) labeled in (b). (c) Simulated ^{27}Al quadrupolar MAS lineshapes for environments I (red) and II (blue) of $AlCl_2^+$ complexed with DCQ (intensities scaled for clarity). (For interpretation of the references to colour in this figure legend, the reader is referred to the web version of this article.)

The total isotropic ^{27}Al shift δ_{iso}^{total} is calculated as the sum of the isotropic chemical shift δ_{iso}^{CS}, the second-order quadrupolar shift δ_{iso}^{2Q}, and the isotropic nucleus-independent chemical shift (NICS) δ_{iso}^{NICS}:

$$\delta_{iso}^{total} = \delta_{iso}^{CS} + \delta_{iso}^{2Q} + \delta_{iso}^{NICS} \quad (1)$$

The quadrupolar coupling constant C_Q is calculated[46] according to

$$C_Q = \frac{eQV_{zz}}{h} \quad (2)$$

where *e* is the elementary charge (e = 1.602x10^{-19}C), *Q* is the nuclear electric quadrupolar moment (*Q* = 148.2 ± 0.5 mb, for ^{27}Al),[47] V_{zz} is the eigenvalue of the EFG tensor with the largest absolute value (by convention, $|V_{zz}| > |V_{yy}| > |V_{xx}|$), and *h* is Planck's constant. The EFG tensor can additionally be described by the quadrupolar asymmetry parameter, η (Equation *(3)*).[46,48,49]

$$\eta = \frac{V_{xx} - V_{yy}}{V_{zz}} \quad (3)$$

The second-order quadrupolar shift δ_{iso}^{2Q} is dependent on C_Q and η: [46,48]

$$\delta_{iso}^{2Q} = -\frac{3}{40}\left(\frac{C_Q}{\omega_L}\right)^2 \frac{I(I+1)-\frac{3}{4}}{I^2(2I-1)^2}\left(1+\frac{\eta^2}{3}\right) \times 10^6 \quad (4)$$

The nucleus-independent chemical shift δ_{iso}^{NICS} reflects the shift induced by ring-current effects from adjacent aromatic molecules.[50] Ring current effects contribute to magnetic shielding and will result in a negative shift. The effect is expected to be greater at small interlayer spacings and as the nucleus of interest moves from the edge to the center of the aromatic ring system. [48,50] These effects will be more significant in larger aromatic systems and are expected to have only minor contributions to the model system studied here.

The isotropic ^{27}Al shifts and quadrupolar coupling constants are highly dependent upon BQ interlayer spacing and lateral displacement of the $AlCl_2^+$ cation. The calculated mean total isotropic ^{27}Al shiftinitially increases with increasing interlayer spacings to a maximum at 5 Å, decreases until 8 Å, before modestly increasing until 10 Å. As discussed above (Equation *(1)*), this shift is a combination of different terms (Fig. S3). Powder XRD measurements of DCQ indicated an interlayer spacing of 3.56 Å for the pristine material, which decreases upon discharge to 3.30 Å (in both $AlCl_3$:[EMIm]Cl, and $AlCl_3$:urea electrolytes) and 3.21 Å (in $AlCl_3$:PA electrolyte) (Fig. S4). From the XRD measurements, the experimental interlayer spacings are thus ca. 3.2–3.3 Å. The calculated total iso-

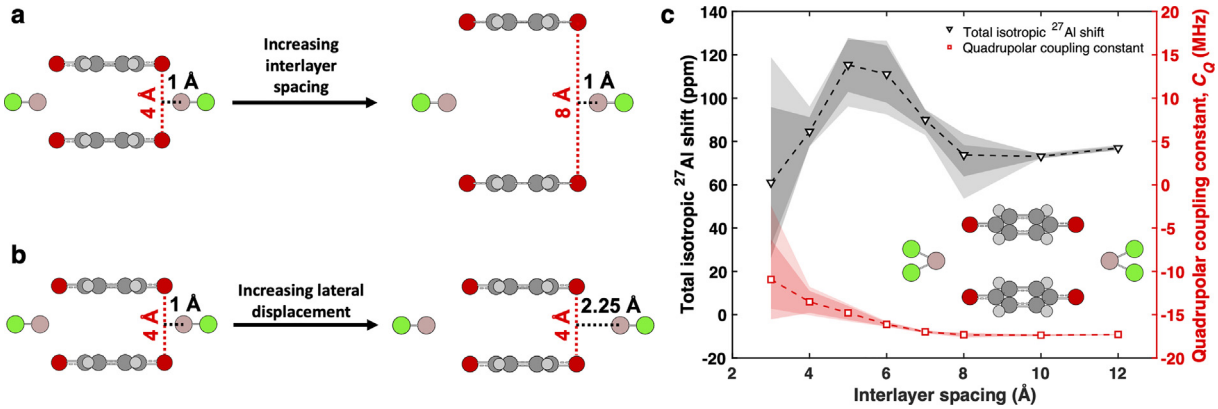

Fig. 7. Schematic of $AlCl_2^+$ cations between two *p*-benzoquinone (BQ) units depicting (a) changing BQ interlayer spacing, and (b) changing $AlCl_2^+$ lateral displacement. (c) Calculated total isotropic ^{27}Al shifts (black triangles) and quadrupolar coupling constants (red squares) of BQ-coordinated $AlCl_2^+$ cations with varying interlayer spacings, each computed for lateral displacements of 1, 1.25, 1.5, 1.75, 2, and 2.25 Å. The mean valued are plotted with ranges and standard deviations shown as lighter and darker shaded regions, respectively. (For interpretation of the references to colour in this figure legend, the reader is referred to the web version of this article.)

tropic ^{27}Al shifts for these interlayer spacings are within the range of the experimentally determined ^{27}Al shifts of 91 and 75 ppm, for Al environments I and II, respectively, and are highly dependent upon lateral spacing (Fig. 7c). The DFT calculations predict that the magnitude of C_Q increases as the quinone layers separate, a direct consequence of a loss of symmetry about the ^{27}Al nucleus as the $AlCl_2^+$ cations move from a tetrahedral geometry to increasingly distorted tetrahedra, and ultimately to an unfavorable two-coordinate geometry. As the interlayer spacing increases, the magnitudes of C_Q converge to a maximum of approximately −17 MHz as the configuration and electronic environment around the ^{27}Al nucleus becomes less influenced by the increasingly distant quinone layers (Fig. 7c). Similarly, the effects of lateral displacement become less significant at higher interlayer spacings, as indicated by the decreasing range and standard deviation. As with the total isotropic ^{27}Al shifts, the experimentally measured C_Q values of 3.5 and 7.7 MHz for environments I and II are within the calculated range of values for an interlayer spacing of ca. 3.2–3.3 Å. While the DFT calculations of this model system do not reveal the precise molecular configurations giving rise to Al environments I and II, they do shed light on the different configurations possible and the variables that affect the ^{27}Al shifts and quadrupolar parameters.

At small interlayer spacings, there are large variations in C_Q and consequently δ_{iso}^{2Q} depending on the lateral spacing of $AlCl_2^+$, which in turn leads to large variations in δ_{iso}^{total}. The variation of interlayer spacings and lateral displacements can be collapsed geometrically into an estimated Al-O bond length since the Al-Cl bond lengths and Cl-Al-Cl bond angles are held constant in the calculations. When the calculated C_Q values were plotted as a function of Al-O bond length and fit to a curve, values of 1.78 and 1.95 Å were obtained for the C_Q values experimentally determined for environments I and II, respectively (Fig. S5a), within the expected range of Al-O bond lengths (1.7–2.2 Å).[51] A similar analysis was performed using the calculated asymmetry parameters as a function of Al-O bond length, where the asymmetry parameters found for environments I and II would correspond to Al-O bond lengths of 2.01 and 2.18 Å, respectively (Fig. S5b). Therefore, the Al–O bond lengths predicted by these analyses fall within the anticipated range, though the magnitudes of ^{27}Al quadrupolar coupling constants calculated for $AlCl_2^+$ between two BQ layers appear to be generally overestimated compared to those experimentally determined in DCQ-$AlCl_2^+$ complexes via solid-state NMR spectroscopy.

Thermochemical Calculations Predict Ion-Generation Pathways. Energies of the electrolyte species and reaction products were also obtained from DFT optimization computations of the relaxed structures, enabling assessment of the most favorable reaction pathway for electroactive cation production via thermochemical calculations. Reaction enthalpies for three pathways of producing $AlCl_2^+$ cations were calculated according to

$$\Delta H^\circ_{rxn} = \sum_{products} \Delta H^\circ_{products} - \sum_{reactants} \Delta H^\circ_{reactants} \quad (5)$$

while the Gibb's free energies were calculated by

$$\Delta G^\circ_{rxn} = \sum_{products} \Delta G^\circ_{products} - \sum_{reactants} \Delta G^\circ_{reactants} \quad (6)$$

The results were calculated at 298.15 K and are tabulated below (Table 1). The experimental reaction product is not an isolated $AlCl_2^+$ cation, but rather $AlCl_2^+$ complexed to electrochemically reduced DCQ; to simulate this effect in a computationally efficient manner, $AlCl_2^+$ was fixed into a tetrahedral geometry, rather than allowing it to relax into a linear geometry. These calculations are thus a first-order approximation though the trends are expected to be generalizable. Reaction energies were also calculated for $Al_2Cl_5^+$ as an alternative cationic reaction product, however, the energies required to produce these ions were far less favorable, while the NMR shifts and C_Q values calculated were in worse agreement with the experimental data (Fig. S6, Table S1).

Reaction #1 is possible in all electrolytes, whereas reactions #2 and #3 are possible only in the ILAs. ΔH°_{rxn} and ΔG°_{rxn} are negative for each reaction and their magnitudes increase from reaction #1 to reaction #3. These reaction energies signify two major outcomes: firstly, the production of $AlCl_2^+$ is energetically favorable, as indicated by the negative Gibb's free energy for all reactions; secondly, that reaction #3 is the most energetically favorable pathway in the ILAs, a result also commensurate with the loss of $Al_2Cl_7^-$ from the electrolyte, as observed in the solid-state ^{27}Al spin-echo NMR spectra of the residual electrolyte in discharged DCQ electrodes (Fig. 4f,i). Note that reactions #2 and #3 involve the generation of neutral ligands (i.e., urea or PA) at the electrochemical interface during the discharge process.

The $Al_2Cl_7^-$ anions are necessary for the efficient electroplating of Al metal, so consumption of this chloroaluminate species can reduce the specific capacity by limiting the charge-compensating electroplating reaction at the anode that occurring during charging:

Table 1
Standard reaction enthalpies and Gibb's free energies required to generate the electroactive $AlCl_2^+$ ions from native electrolyte species at 298.15 K.

		ΔH°_{rxn} (kJ/mol)			ΔG°_{rxn} (kJ/mol)		
#	**Reaction**	**$AlCl_3$:[EMIm]Cl**	**$AlCl_3$:urea**	**$AlCl_3$:PA**	**$AlCl_3$:[EMIm]Cl**	**$AlCl_3$:urea**	**$AlCl_3$:PA**
1	$2Al_2Cl_7^- \rightleftharpoons AlCl_2^+ + 3AlCl_4^-$	−0.7667	−0.7667	−0.7667	−217.2	−217.2	−217.2
2	$AlCl_2L_2^+ \rightleftharpoons AlCl_2^+ + 2L$	–	−163.4	−177.5	–	−389.3	−415.5
3	$Al_2Cl_7^- + AlCl_2L_2^+ \rightleftharpoons AlCl_2^+ + AlCl_4^- + AlCl_3L + L$	–	−219.2	−230.3	–	−434.5	−450.3

$$4Al_2Cl_7^- + 3e^- \rightleftarrows Al + 7AlCl_4^- \quad (7)$$

Thus, if the usable $Al_2Cl_7^-$ is consumed by the cathodic discharge reaction and not replaced, the electrolyte becomes less Lewis acidic, and the battery will cease to charge.

This effect was also probed for the ILA electrolytes, as it has been proposed that aluminum electroplating can occur from the $AlCl_2L_2^+$ cation,[3] for example, according to

$$2\left[AlCl_2 \cdot (urea)_2\right]^+ + 3e^- \rightleftarrows Al + AlCl_4^- + 4(urea) \quad (8)$$

An analogous electrochemical reaction is expected to occur in the $AlCl_3$:PA electrolyte. We tested this hypothesis by attempting to galvanostatically cycle an Al-DCQ cell with a Lewis neutral $AlCl_3$:PA (1:1) electrolyte, where reactions #1 and #3 (Table 1) are not possible due to the absence of $Al_2Cl_7^-$ anions in the electrolyte (Fig. S7). The initial discharge reaction can occur without $Al_2Cl_7^-$, further verifying the feasibility of reaction #2. However, the average discharge potential is ca. 0.53 V and, which is lower than the 1.0 V potential achieved by the Lewis acidic $AlCl_3$:PA (1.3:1) electrolyte, indicating a greater overpotential. While the overpotential can have multiple origins, this observation is consistent with the larger overpotentials measured by Abood et al. using Lewis neutral ILAs [39] and further suggests the favorability of reaction #3 over reaction #2, as indicated by the thermochemical calculations. Importantly, the cell using this Lewis neutral ILA electrolyte was unable to achieve a reasonable charge capacity, resulting in rapid failure in subsequent cycles. As the only $Al_2Cl_7^-$ anions present in the electrolyte would be those generated during discharge, the results also suggest that the aluminum electroplating reaction is much more facile from the $Al_2Cl_7^-$ anion (Equation *(7)*) compared to the $AlCl_2L_2^+$ cation (Equation *(8)*).

In summary, the calculations indicate that the overall electrochemical reaction occurring at DCQ in Lewis acidic $AlCl_3$:[EMIm]Cl ionic liquid is:

$$4Al_2Cl_7^- + DCQ + 2e^- \rightleftarrows DCQ^{2-} \cdot 2AlCl_2^+ + 6AlCl_4^- \quad (9)$$

While the reaction in Equation *(9)* is possible in a Lewis acidic $AlCl_3$:L ionic liquid analogue (L = urea or propionamide), the calculations and experimental results indicate the following electrochemical reaction is most favorable:

$$2Al_2Cl_7^- + 2AlCl_2L_2^+ + DCQ + 2e^- \rightleftarrows DCQ^{2-} \cdot 2AlCl_2^+ + 2AlCl_4^- + 2AlCl_3L + 2L \quad (10)$$

and the following electrochemical reaction can also occur, though is less favored:

$$2AlCl_2L_2^+ + DCQ + 2e^- \rightleftarrows DCQ^{2-} \cdot 2AlCl_2^+ + 4L \quad (11)$$

3. Conclusion

Electrolyte speciation is shown for the first time to significantly impact the molecular-level coordination environments of charge-compensating chloroaluminous ($AlCl_2^+$) cations in rechargeable Al-quinone batteries. DCQ was used as a model anthraquinone-based cathode, while Lewis acidic $AlCl_3$:[EMIm]Cl, $AlCl_3$:urea, and $AlCl_3$:propionamide (PA) electrolytes were used as electrolytes. Solid-state ^{27}Al NMR experiments, including dipolar-mediated and multiple-quantum NMR methods, revealed that charge-compensating $AlCl_2^+$ cations complexed to DCQ exist in two tetrahedral aluminum environments with distinct quadrupolar lineshapes when discharged in $AlCl_3$:[EMIm]Cl and $AlCl_3$:urea electrolytes, whereas only one aluminum environment was observed when using the $AlCl_3$:PA electrolyte. The results establish an electrolyte-dependent ionic charge storage mechanism. This difference may be explained, at least in part, by the impact that the larger propionamide has on the DCQ interlayer spacing, compared to urea. Liquid-state and solid-state ^{27}Al NMR experiments indicated that residual electrolyte in DCQ electrodes discharged in the Lewis acidic $AlCl_3$:urea and $AlCl_3$:PA ionic liquid analogues become Lewis neutral, which significantly affects battery performance. Using a model system composed of $AlCl_2^+$ cations between *p*-benzoquinone layers, DFT computations yielded estimates of ^{27}Al NMR shifts and quadrupolar parameters of $AlCl_2^+$ in different interlayer spacings and lateral displacements, enabling the experimental data to be correlated to its physical origins. Thermochemical calculations identified possible reaction pathways to generate $AlCl_2^+$ from the electrolytes, including the most favorable, revealing in particular the synergistic roles of $Al_2Cl_7^-$ and $AlCl_2L_2^+$ (L = urea, PA) in the electrochemical discharge mechanism in the ionic liquid analogues. The calculations are consistent with galvanostatic cycling of DCQ in a Lewis acidic ionic liquid analogue versus its Lewis neutral equivalent. The results may also be applicable to other multivalent metal–organic battery systems, which often involve complex ion solvation structures and desolvation pathways.

4. Methods

Electrolyte Preparation. The electrolytes were synthesized in an argon-filled glove box (<1.0 ppm of H_2O and O_2). Solutions were prepared by slowly adding $AlCl_3$ (ThermoFisher Scientific, 99.999 %) to 1-ethyl-3-methylimidazolium chloride ([EMIm]Cl; TCI, >98.0 %), urea (Acros Organics, >99.5 %), or propionamide (Acros Organics, 97 %) with constant stirring until the desired molar ratios were achieved (1.5:1, 1.3:1, and 1.3:1, respectively). Due to the exothermic reactions that occur upon addition of $AlCl_3$, the vial was placed in a Peltier thermoelectric cooler (Techne N° - ICE chiller) filled with ceramic-coated cooling beads to regulate temperature and mitigate thermal decomposition during mixing. After addition of $AlCl_3$, the vial was placed on a hot plate at 60 °C and stirred until homogenous.

Composite Electrode Fabrication. 1,5-dichloroanthraquinone (DCQ) electrodes were prepared by ball milling DCQ powder (65 wt%; TCI, >95.0 %) with carbon black (25 wt%; Super P, Alfa Aesar, 99 %) for 1 h. This mixture was combined with poly(tetrafluoroethylene) (PTFE) binder (10 wt%; Aldrich, 1 μm particle size) and mineral spirits were added as required to form a paste (DCQ:Super-P:PTFE mass ratio of 65:25:10). The mixture was calendered at a thickness of approximately 0.5 mm, after which it was then calendered to a final thickness of 110 μm and dried under vacuum

at 60 °C overnight. Final electrode mass loadings were ca. 9.2 mg cm^{-2}.

Cell Assembly. Cells were constructed in PTFE Swagelok unions of 0.25-in. (6.35 mm) and 0.5-in. (12.70 mm) diameters inside an argon-filled glove box (<1.0 ppm of H_2O and O_2). The smaller cells were used for electrochemical measurements, whereas the larger cells were used to harvest electrodes for further characterization. Cells were assembled using a DCQ composite cathode, glass microfiber separator (Whatman GF/D), and aluminum anode (99.99 % Alfa, 0.1-mm thick), with molybdenum current collectors for both electrodes. 6-mm and 11-mm diameter DCQ and aluminum electrodes were used for the 0.25-in. and 0.5-in. Swagelok cells, respectively. 50 μL and 150 μL of electrolyte was used for the smaller and larger cell sizes, respectively. Three-electrode cells for cyclic voltammetry measurements were constructed in 0.25-in. Swagelok cells with an Al wire reference electrode, which was fed through a hole drilled in the center of the PTFE body.

Electrochemical Measurements. Galvanostatic cycling tests were performed in an Arbin Instruments LBT battery cycler using a voltage range of 0.20–1.95 V. Cyclic voltammetry tests were performed at 0.5 mV s^{-1} using a BioLogic VSP-300 potentiostat using a voltage range of 0.05–2.45 V. The open-circuit potential for Al-DCQ cells was approximately 1.3 V after assembly.

X-ray Diffraction. XRD measurements were performed on a PANalytical X'Pert Pro powder diffractometer with a Cu Kα radiation source (λ = 0.544 nm). A scan rate of 0.4° min^{-1} was used to scan a 2θ range of 9.5°– 60°.

Liquid-State NMR Spectroscopy. Liquid-state NMR spectra were acquired on a Bruker AVANCE III HD 300 NMR spectrometer with a 7.05 T narrow-bore (54-mm) bore superconducting magnet equipped with a 5-mm multinuclear broadband fluorine observe (BBFO) probe, operating at 300.13 MHz for ^{1}H and 78.204 MHz for ^{27}Al nuclei. All liquid-state ^{27}Al and ^{1}H single-pulse spectra were acquired under quantitative conditions using (i) a radiofrequency field strength of 25 kHz field strength (π/2 of 10 μs) and 16.7 kHz (π/2 of 15 μs), respectively, and (ii) recycle delays of ≥ 0.5 s and 2-15 s, respectively, which were calibrated such that all nuclear spins relaxed to thermal equilibrium (>5 × T_1, the longitudinal relaxation time). Samples were prepared in an argon-filled glovebox (<1.0 ppm of H_2O and O_2) with coaxial tubes containing an isolated D_2O locking solvent; both tubes sealed with epoxy to ensure no ingress of air upon removal from the glovebox.

Solid-State NMR Spectroscopy. Solid-state NMR spectra were acquired on a Bruker AVANCE III HD 600 NMR spectrometer with a 14.1 T narrow-bore (54-mm) superconducting magnet operating at 600.140 MHz for ^{1}H, 156.378 MHz for ^{27}Al, and 150.910 MHz for ^{13}C nuclei. A Phoenix NMR 1.6-mm HXY magic-angle-spinning (MAS) probehead was used, where all measurements on discharged electrodes were conducted at 40 kHz MAS, while measurements on pristine DCQ were conducted at 35 kHz MAS. Air was pumped through the probehead at 600 L/h and 298.1 K to mitigate MAS-induced sample heating. ^{1}H and ^{13}C shifts were referenced with respect to tetramethylsilane (TMS) at 0 ppm by using adamantane as a secondary chemical shift reference. ^{27}Al shifts were referenced to a 1 M aqueous $Al(NO_3)_3$ solution at 0 ppm.

Solid-state ^{27}Al single-pulse MAS NMR experiments were performed under quantitative conditions by using (i) short π/12 rf pulses (0.31 μs) to ensure linear excitation of all solid and liquid signals and (ii) recycle delays of 0.25-0.40 s such that all ^{27}Al nuclear spins relax to thermal equilibrium (>5 × T_1). ^{27}Al rf pulses were calibrated on 1 M aqueous $Al(NO_3)_3$ where an rf field strength of 135 kHz (π/2 of 1.85 μs) was used for all broadband pulses. ^{27}Al spin-echo experiments were performed using 4 rotor periods in the full-echo delay to optimize liquid signal intensity vs. the solid signal intensity. ^{27}Al{^{1}H} D-HMQC experiments were performed using the $SR4_1^2$ symmetry-based recoupling scheme, which recouples ^{27}Al-^{1}H dipolar interactions while simultaneously decoupling ^{1}H-^{1}H homonuclear interactions. Central-transition (CT) selective pulses used a ^{27}Al rf field strength of 10.4 kHz (π/2 of 24 μs). $SR4_1^2$ recoupling pulses used a ^{1}H rf field strength of 80 kHz (2 × MAS frequency). Preparatory, diverging ^{27}Al double-frequency sweep (DFS) pulses were used to achieve up to three-fold signal enhancements. DFS pulses were swept from 50 kHz to 1 MHz prior to each scan. ^{27}Al{^{27}Al} MQ-MAS experiments were performed using a three-pulse sequence with excitation and conversion rf pulses of 3.5 μs and 1.1 μs, a CT-selective π/2 readout pulse of 24 μs, and a *z*-filter delay of 25 μs. Triple-quantum to single-quantum coherence selection was obtained via phase cycling.

All solid-state ^{1}H NMR experiments used an rf field strength of 161 kHz (π/2 of 1.55 μs) for all broadband pulses. ^{1}H{^{1}H} D-DQF experiments were performed using the BaBa-xy8 scheme for DQ excitation and conversion. The ^{1}H spin-echo experiment performed on pristine DCQ used a 2-rotor-period full-echo delay and was used to eliminate ^{1}H background signals from the probe. ^{13}C{^{1}H} CP-MAS experiments were acquired using a zero-quantum (n = +1) Hartmann-Hahn matching condition achieved by fixing the ^{1}H rf field at 87.5 kHz (5/2 × MAS rate of 35 kHz) and optimizing the ^{13}C spin-locking power around a ^{13}C rf field of 52.5 kHz (3/2 × MAS). CP contact times of 4 ms were used.

Computational Calculations. DFT calculations were performed in Gaussian 09 using the 6-31G+(d,p) basis set and the hybrid B3LYP method (Becke's three-parameter nonlocal exchange functional and Lee – Yang – Parr's correlation functional).[45] Structures with positional constraints were built in Avogadro [52,53] before performing gauge-independent atomic orbital (GIAO) calculations in Gaussian 09 to determine the chemical shielding properties and the electric field gradient (EFG) eigenvalues. The EFG eigenvalues were arranged such that $|V_{xx}|<|V_{yy}|<|V_{zz}|$. To reduce computational expense, structures without constrained positional parameters were first roughly optimized with the UFF forcefield in Avogadro, before being optimized a second time in Gaussian 09 using the 6-31G+(d,p) level of theory. NMR parameters were calculated as discussed above. Chemical shielding was referenced to $Al^{3+}(OH_2)_6$ at 611 ppm.

Data availability

Data will be made available on request.

Declaration of Competing Interest

The authors declare no competing financial interests.

Acknowledgments

The authors gratefully acknowledge support from the U.S. National Science Foundation (NSF) under CAREER award CBET-1847552 and the U.S. National Aeronautics and Space Administration (NASA) via the NASA- CCNY Center for Advanced Batteries for Space under cooperative agreement 80NSSC19M0199. NMR measurements were performed at the City University of New York (CUNY) Advanced Science Research Center. DFT calculations were performed at the CUNY High Performance Computing Center at the College of Staten Island, which is supported in part by NSF awards CNS-0958379, CNS-0855217, ACI- 1126113, and OEC-2215760.

Appendix A. Supplementary data

Supplementary data to this article can be found online at https://doi.org/10.1016/j.jmr.2023.107374.

References

[1] O.M. Leung, T. Schoetz, T. Prodromakis, C. Ponce de Leon, Review—Progress in Electrolytes for Rechargeable Aluminium Batteries, J. Electrochem. Soc. 168 (2021), https://doi.org/10.1149/1945-7111/abfb36.

[2] C. Wang, A. Creuziger, G. Stafford, C.L. Hussey, Anodic Dissolution of Aluminum in the Aluminum Chloride-1-Ethyl-3-methylimidazolium Chloride Ionic Liquid, J. Electrochem. Soc. 163 (2016) H1186–H1194, https://doi.org/10.1149/2.1061614jes.

[3] M. Angell, C.J. Pan, Y. Rong, C. Yuan, M.C. Lin, B.J. Hwang, H. Dai, High Coulombic efficiency aluminum-ion battery using an AlCl3-urea ionic liquid analog electrolyte, Proc. Natl. Acad. Sci. U. S. A. 114 (2017) 834–839, https://doi.org/10.1073/pnas.1619795114.

[4] H. Wang, S. Gu, Y. Bai, S. Chen, F. Wu, C. Wu, High-Voltage and Noncorrosive Ionic Liquid Electrolyte Used in Rechargeable Aluminum Battery, ACS Appl. Mater. Interfaces. 8 (2016) 27444–27448, https://doi.org/10.1021/acsami.6b10579.

[5] X. Han, Y. Bai, R. Zhao, Y. Li, F. Wu, C. Wu, Electrolytes for rechargeable aluminum batteries, Prog. Mater. Sci. 128 (2022), https://doi.org/10.1016/j.pmatsci.2022.100960.

[6] G.A. Elia, K. Marquardt, K. Hoeppner, S. Fantini, R. Lin, E. Knipping, W. Peters, J. F. Drillet, S. Passerini, R. Hahn, An Overview and Future Perspectives of Aluminum Batteries, Adv. Mater. 28 (2016) 7564–7579, https://doi.org/10.1002/adma.201601357.

[7] X. Wen, Y. Liu, A. Jadhav, J. Zhang, D. Borchardt, J. Shi, B.M. Wong, B. Sanyal, R.J. Messinger, J. Guo, Materials Compatibility in Rechargeable Aluminum Batteries: Chemical and Electrochemical Properties between Vanadium Pentoxide and Chloroaluminate Ionic Liquids, Chem. Mater. 31 (2019) 7238–7247, https://doi.org/10.1021/acs.chemmater.9b01556.

[8] D.J. Kim, D.J. Yoo, M.T. Otley, A. Prokofjevs, C. Pezzato, M. Owczarek, S.J. Lee, J. W. Choi, J.F. Stoddart, Rechargeable aluminium organic batteries, Nat. Energy. 4 (2019) 51–59, https://doi.org/10.1038/s41560-018-0291-0.

[9] L.W. Gordon, A.L. Jadhav, M. Miroshnikov, T. Schoetz, G. John, R.J. Messinger, Molecular-Scale Elucidation of Ionic Charge Storage Mechanisms in Rechargeable Aluminum-Quinone Batteries, J. Phys. Chem. C. 126 (2022) 14082–14093, https://doi.org/10.1021/acs.jpcc.2c04272.

[10] D.J. Yoo, J.W. Choi, Elucidating the Extraordinary Rate and Cycling Performance of Phenanthrenequinone in Aluminum-Complex-Ion Batteries, J. Phys. Chem. Lett. 11 (2020) 2384–2392, https://doi.org/10.1021/acs.jpclett.0c00324.

[11] D.J. Yoo, M. Heeney, F. Glöcklhofer, J.W. Choi, Tetradiketone macrocycle for divalent aluminium ion batteries, Nat. Commun. 12 (2021) 1–9, https://doi.org/10.1038/s41467-021-22633-y.

[12] J. Bitenc, N. Lindahl, A. Vizintin, M.E. Abdelhamid, R. Dominko, P. Johansson, Concept and electrochemical mechanism of an Al metal anode - organic cathode battery, Energy Storage Mater. 24 (2020) 379–383, https://doi.org/10.1016/j.ensm.2019.07.033.

[13] N. Lindahl, J. Bitenc, R. Dominko, P. Johansson, Aluminum Metal-Organic Batteries with Integrated 3D Thin Film Anodes, Adv. Funct. Mater. 2004573 (2020) 3–9, https://doi.org/10.1002/adfm.202004573.

[14] L. Zhou, Z. Zhang, L. Cui, F. Xiong, Q. An, Z. Zhou, X.F. Yu, P.K. Chu, K. Zhang, High-capacity and small-polarization aluminum organic batteries based on sustainable quinone-based cathodes with Al3+ insertion, Cell Reports Phys. Sci. 2 (2021), https://doi.org/10.1016/j.xcrp.2021.100354.

[15] M. Mao, Z. Yu, Z. Lin, Y.S. Hu, H. Li, X. Huang, L. Chen, M. Liu, L. Suo, Simplifying and accelerating kinetics enabling fast-charge Al batteries, J. Mater. Chem. A. 8 (2020) 23834–23843, https://doi.org/10.1039/d0ta08348h.

[16] Y. Liu, W. Luo, S. Lu, Z. Zhang, Z. Chao, J. Fan, Novel Carbonyl Cathode for Green and Sustainable Aluminum Organic Batteries, ACS Appl. Mater. Interfaces. (2022), https://doi.org/10.1021/acsami.2c14365.

[17] Y.T. Kao, S.B. Patil, C.Y. An, S.K. Huang, J.C. Lin, T.S. Lee, Y.C. Lee, H.L. Chou, C.W. Chen, Y.J. Chang, Y.H. Lai, D.Y. Wang, A Quinone-Based Electrode for High-Performance Rechargeable Aluminum-Ion Batteries with a Low-Cost AlCl3/Urea Ionic Liquid Electrolyte, ACS Appl. Mater. Interfaces. 12 (2020) 25853–25860, https://doi.org/10.1021/acsami.0c04640.

[18] G. Wang, E. Dmitrieva, B. Kohn, U. Scheler, Y. Liu, V. Tkachova, L. Yang, Y. Fu, J. Ma, P. Zhang, F. Wang, J. Ge, X. Feng, An Efficient Rechargeable Aluminium-Amine Battery Working Under Quaternization Chemistry, Angew. Chemie - Int. Ed. 61 (2022), https://doi.org/10.1002/anie.202116194.

[19] Z. Yang, F. Wang, P. Meng, J. Luo, C. Fu, Recent advances in developing organic positive electrode materials for rechargeable aluminum-ion batteries, Energy Storage Mater. 51 (2022) 63–79, https://doi.org/10.1016/j.ensm.2022.06.018.

[20] M. Malik, K.L. Ng, G. Azimi, Physicochemical characterization of AlCl3-urea ionic liquid analogs: Speciation, conductivity, and electrochemical stability, Electrochim. Acta. 354 (2020), https://doi.org/10.1016/j.electacta.2020.136708.

[21] T. Whewell, V.R. Seymour, K. Griffiths, N.R. Halcovitch, A.V. Desai, R.E. Morris, A.R. Armstrong, J.M. Griffin, A structural investigation of organic battery anode materials by NMR crystallography, Magn. Reson. Chem. 60 (2022) 489–503, https://doi.org/10.1002/mrc.5249.

[22] C.M. Widdifield, R.W. Schurko, Understanding chemical shielding tensors using group theory, MO analysis, and modern density-functional theory, Concepts Magn, Reson. Part A Bridg. Educ. Res. 34 (2009) 91–123, https://doi.org/10.1002/cmr.a.20136.

[23] J. Autschbach, S. Zheng, R.W. Schurko, Analysis of electric field gradient tensors at quadrupolar nuclei in common structural motifs, Concepts Magn. Reson. Part A. 36A (2010) 84–126, https://doi.org/10.1002/cmr.a.20155.

[24] R.W. Schurko, R.E. Wasylishen, A.D. Phillips, A Definitive Example of Aluminum-27 Chemical Shielding Anisotropy, J. Magn. Reson. 133 (1998) 388–394, https://doi.org/10.1006/jmre.1998.1460.

[25] R. Jay, A.L. Jadhav, L.W. Gordon, R.J. Messinger, Soluble Electrolyte-Coordinated Sulfide Species Revealed in Al–S Batteries by Nuclear Magnetic Resonance Spectroscopy, Chem. Mater. 34 (2022) 4486–4495, https://doi.org/10.1021/acs.chemmater.2c00248.

[26] J. He, X. Shi, C. Wang, H. Zhang, X. Liu, Z. Yang, X. Lu, A quinone electrode with reversible phase conversion for long-life rechargeable aqueous aluminum-metal batteries, Chem. Commun. 57 (2021) 6931–6934, https://doi.org/10.1039/d1cc02024b.

[27] D. Paterno, E. Rock, A. Forbes, R. Iqbal, N. Mohammad, S. Suarez, Aluminum ions speciation and transport in acidic deep eutectic AlCl3 amide electrolytes, J. Mol. Liq. 319 (2020), https://doi.org/10.1016/j.molliq.2020.114118.

[28] K. Saalwächter, F. Lange, K. Matyjaszewski, C.F. Huang, R. Graf, BaBa-xy16: Robust and broadband homonuclear DQ recoupling for applications in rigid and soft solids up to the highest MAS frequencies, J. Magn. Reson. 212 (2011) 204–215, https://doi.org/10.1016/j.jmr.2011.07.001.

[29] A. Brinkmann, A.P.M. Kentgens, Proton-selective 17O–1H distance measurements in fast magic-angle-spinning solid-state NMR spectroscopy for the determination of hydrogen bond lengths, J. Am. Chem. Soc. 128 (2006) 14758–14759, https://doi.org/10.1021/ja065415k.

[30] M.H. Levitt, Symmetry-Based Pulse Sequences in Magic-Angle Spinning Solid-State NMR, in: Encycl. Magn. Reson., John Wiley & Sons, Ltd, Chichester, UK, 2007: pp. 165–196. https://doi.org/10.1002/9780470034590.emrstm0551.

[31] H. Dong, O. Tutusaus, Y. Liang, Y. Zhang, Z. Lebens-Higgins, W. Yang, R. Mohtadi, Y. Yao, High-power Mg batteries enabled by heterogeneous enolization redox chemistry and weakly coordinating electrolytes, Nat. Energy. 5 (2020) 1043–1050, https://doi.org/10.1038/s41560-020-00734-0.

[32] S. Voskian, T.A. Hatton, Faradaic electro-swing reactive adsorption for CO2 capture, Energy Environ. Sci. 12 (2019) 3530–3547, https://doi.org/10.1039/c9ee02412c.

[33] C. Ferrara, V. Dall'Asta, V. Berbenni, E. Quartarone, P. Mustarelli, Physicochemical Characterization of AlCl3-1-Ethyl-3-methylimidazolium Chloride Ionic Liquid Electrolytes for Aluminum Rechargeable Batteries, J. Phys. Chem. C. 121 (2017) 26607–26614. https://doi.org/10.1021/acs.jpcc.7b07562.

[34] C. Liu, W. Chen, Z. Wu, B. Gao, X. Hu, Z. Shi, Z. Wang, Density, viscosity and electrical conductivity of AlCl3-amide ionic liquid analogues, J. Mol. Liq. 247 (2017) 57–63, https://doi.org/10.1016/j.molliq.2017.09.091.

[35] S.K. Noh, J.H. Jeon, W.J. Jang, H. Kim, S.H. Lee, M.W. Lee, J. Lee, S. Han, S.J. Kahng, Supramolecular Cl×××H and O×××H interactions in self-assembled 1,5-dichloroanthraquinone layers on Au(111), ChemPhysChem. 14 (2013) 1177–1181, https://doi.org/10.1002/cphc.201201061.

[36] Y. Berger, M. Berger-Deguée, A. Castonguay, Carbon-13 nuclear magnetic resonance studies of anthraquinones. IV—correlation of substituent effects for 1-substituted anthraquinones, Org. Magn. Reson. 15 (1981) 303–306, https://doi.org/10.1002/mrc.1270150319.

[37] J.S. Wilkes, J.S. Frye, G.F. Reynolds, 27A1 and 13C NMR Studies of Aluminum Chloride-Dialkylimidazolium Chloride Molten Salts, Inorg. Chem. 22 (1983) 3870–3872, https://doi.org/10.1021/ic00168a011.

[38] M. Angell, G. Zhu, M.C. Lin, Y. Rong, H. Dai, Ionic Liquid Analogs of AlCl3 with Urea Derivatives as Electrolytes for Aluminum Batteries, Adv. Funct. Mater. 30 (2020) 1–11, https://doi.org/10.1002/adfm.201901928.

[39] H.M.A. Abood, A.P. Abbott, A.D. Ballantyne, K.S. Ryder, Do all ionic liquids need organic cations? Characterisation of [AlCl2·nAmide]+ AlCl4- and comparison with imidazolium based systems, Chem. Commun. 47 (2011) 3523–3525, https://doi.org/10.1039/c0cc04989a.

[40] M. Li, B. Gao, C. Liu, W. Chen, Z. Wang, Z. Shi, X. Hu, AlCl3/amide ionic liquids for electrodeposition of aluminum, J. Solid State Electrochem. 21 (2017) 469–476, https://doi.org/10.1007/s10008-016-3384-3.

[41] D. Fenzke, D. Freude, T. Fröhlich, J. Haase, NMR intensity measurements of half-integer quadrupole nuclei, Chem. Phys. Lett. 111 (1984) 171–175, https://doi.org/10.1016/0009-2614(84)80458-3.

[42] A.L. Jadhav, J.H. Xu, R.J. Messinger, Quantitative molecular-level understanding of electrochemical aluminum-ion intercalation into a crystalline battery electrode, ACS Energy Lett. 5 (2020) 2842–2848, https://doi.org/10.1021/acsenergylett.0c01138.

[43] M.A. Hope, K.J. Griffith, B. Cui, F. Gao, S.E. Dutton, S.S.P. Parkin, C.P. Grey, The Role of Ionic Liquid Breakdown in the Electrochemical Metallization of VO 2: An NMR Study of Gating Mechanisms and VO 2 Reduction, J. Am. Chem. Soc. 140 (2018) 16685–16696, https://doi.org/10.1021/jacs.8b09513.

[44] D. Massiot, F. Fayon, M. Capron, I. King, S. Le Calvé, B. Alonso, J.O. Durand, B. Bujoli, Z. Gan, G. Hoatson, Modelling one- and two-dimensional solid-state NMR spectra, Magn. Reson. Chem. 40 (2002) 70–76, https://doi.org/10.1002/mrc.984.

[45] M.J. Frisch, G.W. Trucks, H.B. Schlegel, G.E. Scuseria, M.A. Robb, J.R. Cheeseman, G. Scalmani, V. Barone, B. Mennucci, G.A. Petersson, H. Nakatsuji, M. Caricato, X. Li, H.P. Hratchian, A.F. Izmaylov, J. Bloino, G. Zheng, J.L. Sonnenberg, M. Hada, M. Ehara, K. Toyota, R. Fukuda, J. Hasegawa, M. Ishida, T. Nakajima, Y. Honda, O. Kitao, H. Nakai, T. Vreven, J.A. Montgomery Jr., J.E. Peralta, F. Ogliaro, M. Bearpark, J.J. Heyd, E. Brothers, K.N. Kudin, V.N. Staroverov, R. Kobayashi, J. Normand, K. Raghavachari, A. Rendell, J.C. Burant, S.S. Iyengar, J. Tomasi, M. Cossi, N. Rega, J.M. Millam, M. Klene, J.E. Knox, J.B. Cross, V. Bakken, C. Adamo, J. Jaramillo, R. Gomperts, R.E. Stratmann, O. Yazyev, A.J. Austin, R. Cammi, C.

Pomelli, J.W. Ochterski, R.L. Martin, K. Morokuma, V.G. Zakrzewski, G.A. Voth, P. Salvador, J.J. Dannenberg, S. Dapprich, A.D. Daniels, Ö. Farkas, J.B. Foresman, J. V Ortiz, J. Cioslowski, D.J. Fox, Gaussian 09 Revision E.01, (2009).

[46] J. Cuny, S. Messaoudi, V. Alonzo, E. Furet, J.-F. Halet, E. Le Fur, S.E. Ashbrook, C.J. Pickard, R. Gautier, L. Le Polles, DFT calculations of quadrupolar solid-state NMR properties: Some examples in solid-state inorganic chemistry, J. Comput. Chem. 29 (2008) 2279–2287, https://doi.org/10.1002/jcc.21028.

[47] A. Aerts, A. Brown, A revised nuclear quadrupole moment for aluminum: Theoretical nuclear quadrupole coupling constants of aluminum compounds, J. Chem. Phys. 150 (2019), https://doi.org/10.1063/1.5097151.

[48] J.H. Xu, A.L. Jadhav, D.E. Turney, R.J. Messinger, Molecular-level environments of intercalated chloroaluminate anions in rechargeable aluminum-graphite batteries revealed by solid-state NMR spectroscopy, J. Mater. Chem. A. 8 (2020) 16006–16017, https://doi.org/10.1039/d0ta02611e.

[49] L.J. Criscenti, S.L. Brantley, K.T. Mueller, N. Tsomaia, J.D. Kubicki, Theoretical and 27Al CPMAS NMR investigation of aluminum coordination changes during aluminosilicate dissolution, Geochim. Cosmochim. Acta. 69 (2005) 2205–2220, https://doi.org/10.1016/j.gca.2004.10.020.

[50] A.C. Forse, J.M. Griffin, V. Presser, Y. Gogotsi, C.P. Grey, Ring current effects: Factors affecting the NMR chemical shift of molecules adsorbed on porous carbons, J. Phys. Chem. C. 118 (2014) 7508–7514, https://doi.org/10.1021/jp502387x.

[51] E. Lam, A. Comas-Vives, C. Copéret, Role of Coordination Number, Geometry, and Local Disorder on 27Al NMR Chemical Shifts and Quadrupolar Coupling Constants: Case Study with Aluminosilicates, J. Phys. Chem. C. 121 (2017) 19946–19957, https://doi.org/10.1021/acs.jpcc.7b07872.

[52] M.D. Hanwell, D.E. Curtis, D.C. Lonie, T. Vandermeersch, E. Zurek, G.R. Hutchison, Avogadro: an advanced semantic chemical editor, visualization, and analysis platform, J. Cheminform. 4 (2012) 17, https://doi.org/10.1186/1758-2946-4-17.

[53] Avogadro Chemistry, Avogadro: an open-source molecular builder and visualization tool. Version 1.2.0, (2016). http://avogadro.cc/.